Processing Map of NiTiNb Shape Memory Alloy Subjected to Plastic Deformation at High Temperatures

Yu Wang [1,2], Shuyong Jiang [1,*] and Yanqiu Zhang [1]

[1] College of Mechanical and Electrical Engineering, Harbin Engineering University, Harbin 150001, China; wangyuhrbeu@126.com (Y.W.); zhangyq@hrbeu.edu.cn (Y.Z.)

[2] College of Materials Science and Chemical Engineering, Harbin Engineering University, Harbin 150001, China

* Correspondence: jiangshuyong@hrbeu.edu.cn; Tel.: +86-451-8251-9710

Abstract: The processing map of $Ni_{47}Ti_{44}Nb_9$ (at %) shape memory alloy (SMA), which possesses B2 austenite phases and β-Nb phases at room temperature, is established in order to optimize the hot working parameters. Based on true stress-strain curves of NiTiNb SMA during uniaxial compression deformation at the temperatures ranging from 700 to 1000 °C and at the strain rates ranging from 0.0005 to 0.5 s^{-1}, according to dynamic material model (DMM) principle, the processing map of NiTiNb SMA is obtained on the basis of power dissipation map and instability map. The instability region of NiTiNb SMA increases with increasing the true strain and it mainly focuses on the region with high strain rate. The workability of NiTiNb SMA becomes worse and worse with increasing plastic strain, as well as decreasing deformation temperature. There exist two stability zones which are suitable for hot working of NiTiNb SMA. In one stability region, the deformation temperature ranges from 750 to 840 °C and the strain rate ranges from 0.0003 to 0.001 s^{-1}. In the other stability region, the deformation temperature ranges from 930 to 1000 °C and the strain rate ranges from 0.016 to 0.1 s^{-1}. The severe microstructure defects, such as coarsening grains, band microstructure, and intercrystalline overfiring appear in the microstructures of NiTiNb SMA which is subjected to plastic deformation in the instability zone.

Keywords: shape memory alloy; NiTiNb alloy; plastic deformation; processing map

1. Introduction

Binary NiTi shape memory alloy (SMA) has been extensively used in the engineering field due to its unique phenomena, which include a shape memory effect and superelasticity [1–3]. It is of great importance to add the third element to the binary NiTi SMA so as to broaden the engineering application [4–6]. As a typical example, the addition of Nb element to the binary NiTi SMA contributes to enhancing phase transformation temperature hysteresis [7,8]. In particular, when the soft β-Nb phase in the NiTiNb SMA suffers from plastic deformation, the relaxation of elastic strain in the martensite interface contributes to lowering the driving force of reverse martensite transformation and, hence, facilitating the stability of martensite [9]. Therefore, NiTiNb SMA has been a perfect candidate for pipe coupling because the large phase transformation temperature hysteresis plays a predominant role in guaranteeing the reliability of pipe coupling in engineering applications [10–12].

It is well known that hot working, especially high-temperature plastic deformation, is an indispensable means to manufacture the product of NiTi-based SMAs [13–15]. Furthermore, it is of great importance in improving the microstructures and the properties of NiTi-based SMAs, as well [16–18]. Therefore, it is very necessary to explore an effective tool for optimizing the process

parameters, which are suitable for hot working of NiTi-based SMAs. As we know, the processing map has been a reliable and effective tool to help optimize the hot working parameters of metal materials [19–23]. So far, no literature has reported the involved information with respect to processing maps of NiTiNb SMA. Therefore, in the present study, uniaxial compression deformation of $Ni_{47}Ti_{44}Nb_9$ (at %) SMA is carried out at the temperatures ranging from 600 to 1000 °C and at strain rates ranging from 0.0005 to 0.5 s^{-1}. The processing map of NiTiNb SMA is established according to dynamic material model (DMM) theory [24].

2. Materials and Methods

The commercially as-rolled $Ni_{47}Ti_{44}Nb_9$ (at %) SMA bar, which possesses the diameter of 20 mm, was obtained from Xi'an Saite Metal Materials Development Co., Ltd. (Xi'an, China). The phase composition of as-rolled NiTiNb SMA was characterized by X-ray diffraction (XRD) testing using a Philips X'Pert Pro diffractometer (Royal Dutch Philips Electronics Ltd., Amsterdam, The Netherlands) with CuKα radiation at ambient temperature. The involved sample was scanned on the basis of 2θ ranging from 20° to 90° by means of continuous scanning based on a tube voltage of 40 kV and tube current of 40 mA. Figure 1 shows the XRD diagram of the as-rolled NiTiNb SMA, where NiTiNb SMA consists of B2 austenite and β-Nb phases.
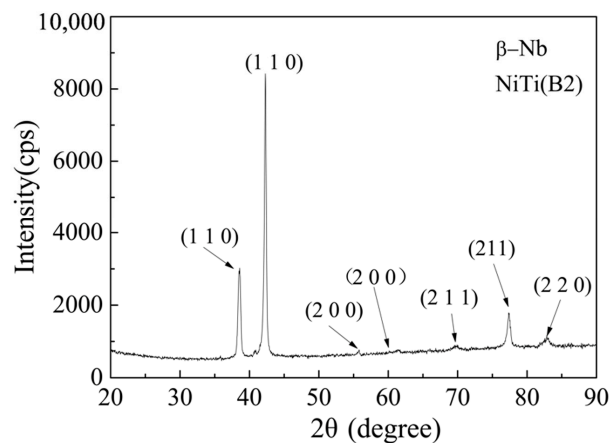

Figure 1. XRD map of as-rolled NiTiNb SMA.

Sixteen NiTiNb SMA samples, which possess diameters of 6 mm and heights of 9 mm, were removed from the as-rolled NiTiNb SMA bar using electro-discharge machining (EDM, DK7725, Jiangsu Dongqing CNC Machine Tool Co., Ltd., Taizhou, China). The NiTiNb SMA samples were placed between the top anvil and the bottom one of an INSTRON-5500R equipment (Instron Corporation, Norwood, MA, USA). Subsequently, they were compressed by the deformation degree of 60% at temperatures ranging from 700 to 1000 °C and at strain rates ranging from 0.0005 to 0.5 s^{-1}.

Optical microscopy (OM) observation was used to investigate the microstructures of as-rolled and compressed NiTiNb SMA samples by means of an OLYMPUS 311 (Olympus Corporation, Tokyo, Japan) optical microscope. The sample for OM observation was etched in a solution of HF:HNO$_3$:H$_2$O = 1:3:10. The microstructure of as-rolled NiTiNb SMA is shown in Figure 2. It can be observed that the as-rolled NiTiNb SMA exhibits a homogeneous worm-like microstructure.
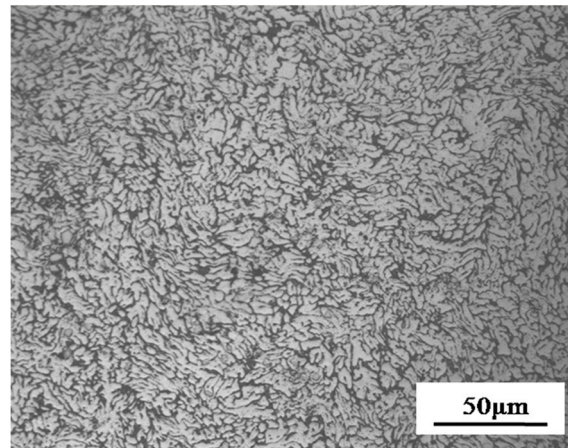
Figure 2. Microstructures of as-rolled NiTiNb SMA.

3. Principle for the Processing Map

A processing map of NiTiNb SMA is established on the basis of dynamic material model (DMM). According to DMM, when NiTiNb SMA is subjected to plastic deformation at high temperatures, the dissipation power P is composed of two parts. One part deals with the power (G) consumed due to plastic deformation and the other part refers to the energy (J) dissipated due to microstructural evolution. Therefore, the dissipation power P is expressed by [25]:

$$P = \sigma \cdot \dot{\varepsilon} = G + J = \int_0^{\dot{\varepsilon}} \sigma d\dot{\varepsilon} + \int_0^{\sigma} \dot{\varepsilon} d\sigma \qquad (1)$$

where G is defined as the dissipated content and J refers to the dissipated co-content.

When strain ε and temperature T are unchangeable, stress σ is regarded as a function of the strain rate $\dot{\varepsilon}$, which is described as a power law relationship [26–28], namely:

$$\sigma = K\dot{\varepsilon}^m \qquad (2)$$

where K refers to material coefficient and m stands for strain rate sensitivity. The value of m is expressed as:

$$m = \frac{dJ}{dG} = \frac{\dot{\varepsilon} d\sigma}{\sigma d\dot{\varepsilon}} = \frac{\dot{\varepsilon}\sigma d\ln\sigma}{\sigma\dot{\varepsilon} d\ln\dot{\varepsilon}} \approx \frac{\Delta \lg\sigma}{\Delta \lg\dot{\varepsilon}} \qquad (3)$$

When strain ε and temperature T are constant, the dissipated co-content J is represented by:

$$J = \int_0^{\sigma} \dot{\varepsilon} d\sigma = \frac{m\sigma\dot{\varepsilon}}{m+1} \qquad (4)$$

In general, the m value shows a linear dependence on the temperature T and the strain rate $\dot{\varepsilon}$. The metal material is considered to be an ideal linear dissipation state if the value of m is taken as 1. Then, the dissipated co-content J reaches the maximum value $J_{\max}$ [29], namely:

$$J_{\max} = \frac{\sigma\dot{\varepsilon}}{2} \qquad (5)$$

Consequently, according to Equations (4) and (5), the power dissipation efficiency η is expressed as follows:

$$\eta = \frac{J}{J_{\max}} = \frac{2m}{m+1} \qquad (6)$$

where η depends on temperature T, strain ε and strain rate $\dot{\varepsilon}$. In the case of a constant strain, the power dissipation map is established by drawing a contour map of η versus the strain rate $\dot{\varepsilon}$ and temperature T.

The power dissipation map is indicative of the microstructural evolution law resulting from the dissipated energy of the material. In general, the power dissipation map is of great importance in terms of determining the workability of metal material. However, the workability of metal material is not completely dependent on the power dissipation map since there is a larger η value in a region where the workability of metal material is very poor. Therefore, it is necessary to use a judging criterion for evaluating the workability of metal material. According to the maximum entropy principle, the unstable flow occurs during plastic deformation of metal material when the following equation is satisfied [30], namely:

$$\frac{\mathrm{d}D}{\mathrm{d}\dot{\varepsilon}} < \frac{D}{\dot{\varepsilon}} \tag{7}$$

where D is the power dissipation function, which depends on the specific temperature. If the total power is dissipated, D is identical to P. Based on DMM, if the partition in Equation (1) leads to the different instability parameters, D is identical to J. As a consequence, Equation (7) is expressed as:

$$\frac{\mathrm{d}J}{\mathrm{d}\dot{\varepsilon}} < \frac{J}{\dot{\varepsilon}} \tag{8}$$

According to the mathematical transformation, Equation (8) is expressed by:

$$\frac{\mathrm{d}J}{\mathrm{d}\dot{\varepsilon}} = \frac{J\dot{\varepsilon}}{\dot{\varepsilon}J} \cdot \frac{\mathrm{d}J}{\mathrm{d}\dot{\varepsilon}} = \frac{J}{\dot{\varepsilon}} \cdot \frac{\mathrm{d}(\int (1/J)dJ)}{\mathrm{d}(\int (1/\dot{\varepsilon})d\dot{\varepsilon})} = \frac{J}{\dot{\varepsilon}} \cdot \frac{\mathrm{dlg}J}{\mathrm{dlg}\dot{\varepsilon}} \tag{9}$$

By combining Equation (9) with Equation (8), the following equation is acquired, namely:

$$\frac{\mathrm{dlg}J}{\mathrm{dlg}\dot{\varepsilon}} < 1 \tag{10}$$

Then, the substitution of Equation (4) into Equation (10) results in:

$$\frac{\mathrm{dlg}J}{\mathrm{dlg}\dot{\varepsilon}} = \frac{\mathrm{dlg}(m/m+1)}{\mathrm{dlg}\dot{\varepsilon}} + \frac{\mathrm{dlg}\sigma}{\mathrm{dlg}\dot{\varepsilon}} + \frac{\mathrm{dlg}\dot{\varepsilon}}{\mathrm{dlg}\dot{\varepsilon}} < 1 \tag{11}$$

As a result, the criterion judging the unstable flow of metal material during plastic deformation is expressed as follows [31]:

$$\xi(\dot{\varepsilon}) = \frac{\partial \lg\left(\frac{m}{m+1}\right)}{\partial \lg\dot{\varepsilon}} + m < 0 \tag{12}$$

where the instability parameter $\xi(\dot{\varepsilon})$ depends on m and $\dot{\varepsilon}$. In addition, m relies on T and $\dot{\varepsilon}$. Accordingly, $\xi(\dot{\varepsilon})$ is dependent upon T and $\dot{\varepsilon}$. As for a given strain, the instability map is constructed by plotting a contour map of $\xi(\dot{\varepsilon})$ versus $\dot{\varepsilon}$ and T. In general, $\xi(\dot{\varepsilon})$ is negative in the zone where metal material presents an unstable flow during plastic deformation. Therefore, the instability region is identified by means of the instability map. Finally, the processing map is established on the basis of the instability map and the power dissipation map.

4. Results and Discussion

Figure 3 indicates the true stress-strain curves of NiTiNb SMA undergoing uniaxial compression at the temperatures ranging from 700–1000 °C and at the strain rates ranging from 0.0005–0.5 s^{-1}. It is evident that flow stress is dependent upon the strain rate and temperature. In the case of a constant strain rate, the flow stress decreases with increasing temperature. As for a constant temperature, the flow stress increases with increasing strain rate. According to the various temperatures and strain

rates, the values of flow stresses, which correspond to the true strains of 0.3, 0.6, and 0.9, respectively, are extracted from the true stress-strain data, as shown in Table 1.
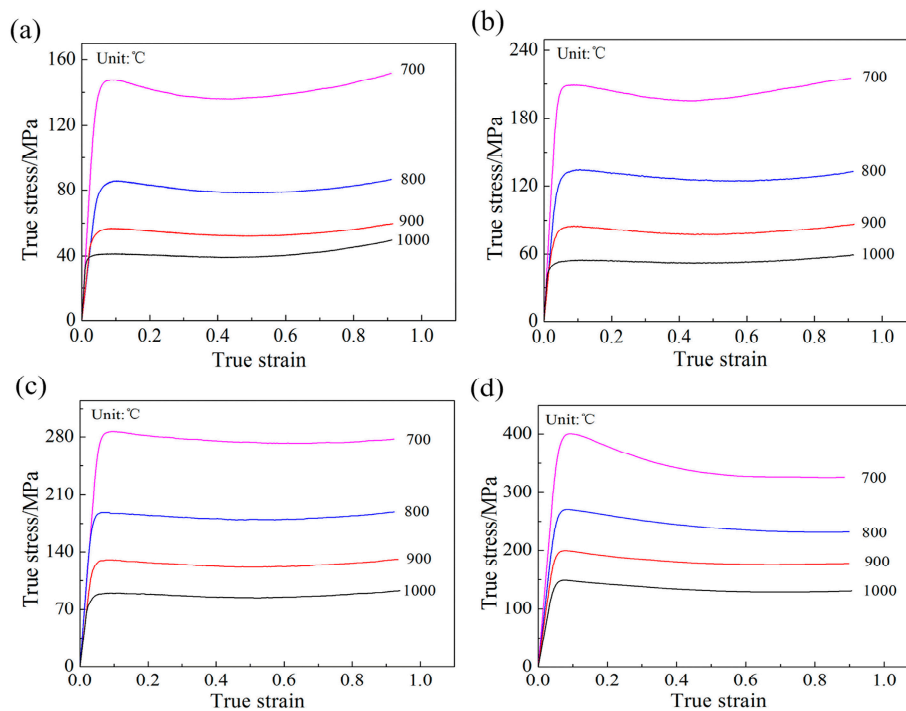

Figure 3. True stress-strain curves of NiTiNb SMA undergoing uniaxial compression based on the various temperatures and strain rates: (**a**) $\dot{\varepsilon} = 0.0005$ s^{-1}; (**b**) $\dot{\varepsilon} = 0.005$ s^{-1}; (**c**) $\dot{\varepsilon} = 0.05$ s^{-1}; and (**d**) $\dot{\varepsilon} = 0.5$ s^{-1}.

Table 1. Flow stresses of NiTiNb SMA (MPa).

ε	$\dot{\varepsilon}/s^{-1}$	$T/°C$			
		700	800	900	1000
0.3	0.0005	137.8010	80.4978	53.4650	39.7838
	0.005	199.2236	128.6067	79.6107	53.3478
	0.05	278.4276	182.6738	124.5443	87.1276
	0.5	362.9075	254.1071	185.9302	139.1716
0.6	0.0005	138.6029	78.6816	52.6534	40.1727
	0.005	199.7022	124.5523	78.5104	53.1897
	0.05	272.5415	179.6717	121.7723	85.0241
	0.5	328.3940	236.2028	176.2441	130.1123
0.9	0.0005	150.7980	85.8143	59.2176	48.7737
	0.005	214.5237	131.7976	85.6582	58.8096
	0.05	276.0619	187.4464	129.4072	91.1164
	0.5	325.8891	231.8062	177.1036	130.8063

According to the experimental data shown in Table 1, the curve of lgσ versus lg$\dot{\varepsilon}$ can be obtained by means of the linear fitting method, as shown in Figure 4. It is evident that there is an approximate linear relationship between lgσ and lg$\dot{\varepsilon}$. The approximate linear relationship indicates that NiTiNb SMA satisfies the conditions of DMM during plastic deformation.
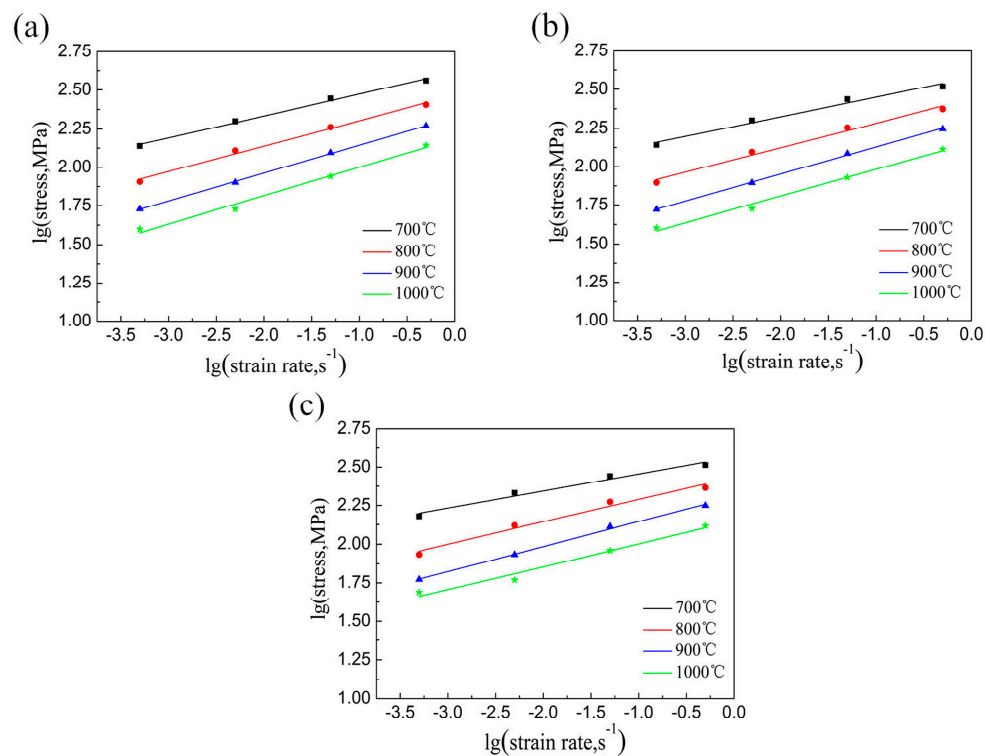
Figure 4. Linear relationship between $\log \sigma$ and $\log \dot{\varepsilon}$ based on various strains: (**a**) $\varepsilon = 0.3$; (**b**) $\varepsilon = 0.6$; and (**c**) $\varepsilon = 0.9$.

By performing cubic-spline fitting based on the aforementioned data, the fitted curves of $\lg \sigma$ versus $\lg \dot{\varepsilon}$ are acquired. Then, according to Equation (3), a series of *m* values are obtained by identifying the slopes of these fitted curves. Consequently, according to Equation (6), the power dissipation efficiency η is calculated at various plastic strains. Furthermore, the power dissipation maps of NiTiNb SMA based on various strains are obtained, as shown in Figure 5. On the one hand, the power dissipation maps are able to reflect relative variation rate of internal entropy in the metal material subjected to hot plastic deformation. On the other hand, the power dissipation maps can be used for roughly estimating the microstructure change of metal material undergoing plastic deformation at the various temperatures and strain rates. In general, the higher η values mean that the deformed microstructures probably possess better performance. It is noted that the value of η approximately increases with increasing deformation temperature, whereas it decreases with increasing strain rate. It can be found that, in the whole temperature range, there exist two regions where η possesses a peak value. One region is involved in the temperature range of 750–840 °C, as well as the strain rate range of 0.0003~0.001 s^{-1}. The other region deals with the temperature range of 930–1000 °C as well as the strain rate range of 0.016–0.1 s^{-1}. In addition, the maximum value of η decreases with increasing true strain. The phenomenon indicates that the hot workability of NiTiNb SMA becomes worse and worse along with the increase in plastic strain.
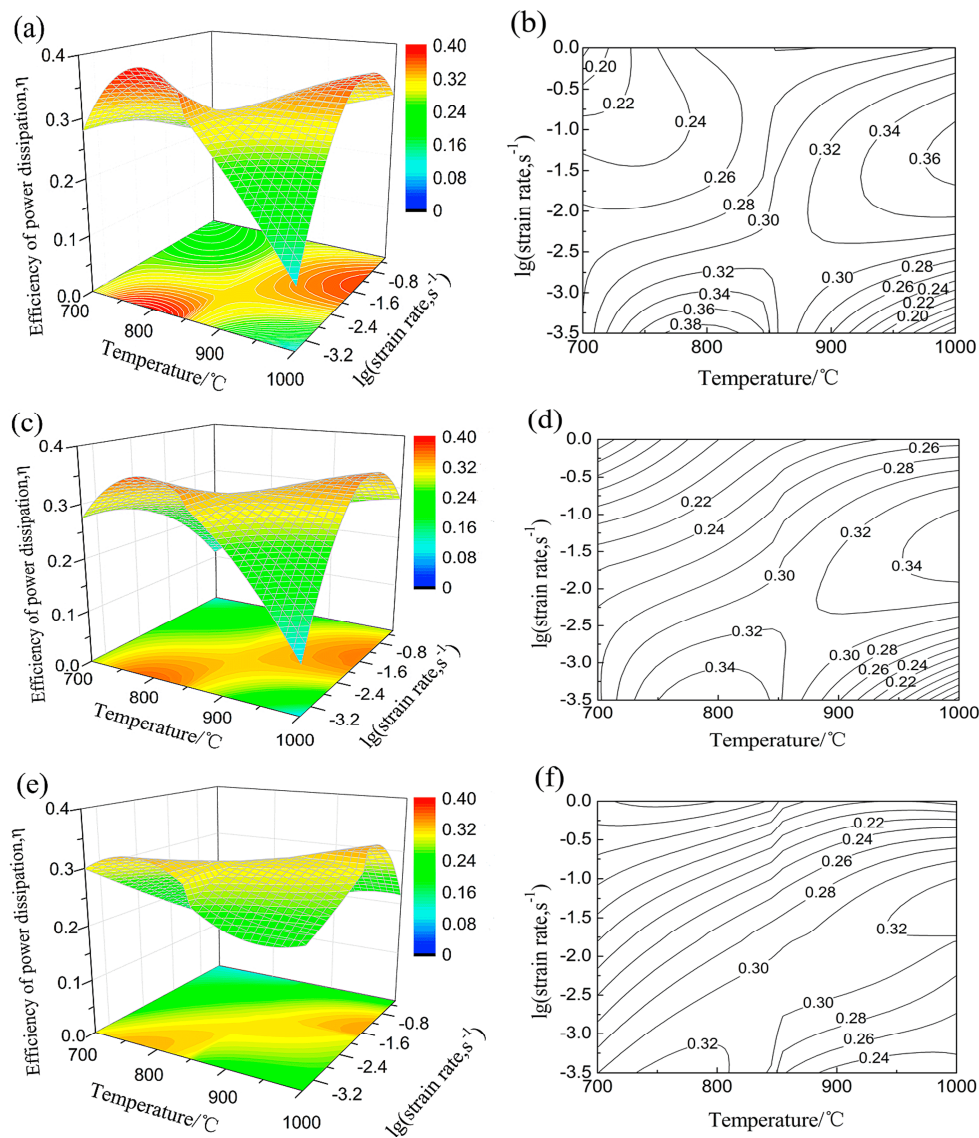
Figure 5. Power dissipation maps of NiTiNb SMA based on various strains: (**a**) $\varepsilon = 0.3$, 3D surface map; (**b**) $\varepsilon = 0.3$, 2D contour line map; (**c**) $\varepsilon = 0.6$, 3D surface map; (**d**) $\varepsilon = 0.6$, 2D contour line map; (**e**) $\varepsilon = 0.9$, 3D surface map; and (**f**) $\varepsilon = 0.9$, 2D contour line map.

The values of $\xi(\dot{\varepsilon})$ under the various deformation conditions can be calculated by combining Equations (3) and (12). As a consequence, the instability maps are established, as shown in Figure 6. In general, the region where $\xi(\dot{\varepsilon})$ possesses negative values in the instability maps is defined as the instability region where metal material exhibits an unstable flow during plastic deformation. In a similar manner, the region where $\xi(\dot{\varepsilon})$ possesses positive values in the instability maps is defined as the stability region where metal material shows a stable flow during plastic deformation. It is observed from Figure 6 that the unstable flow mainly appears in the zone possessing high strain rate. Furthermore, the instability region increases with increasing true strain.
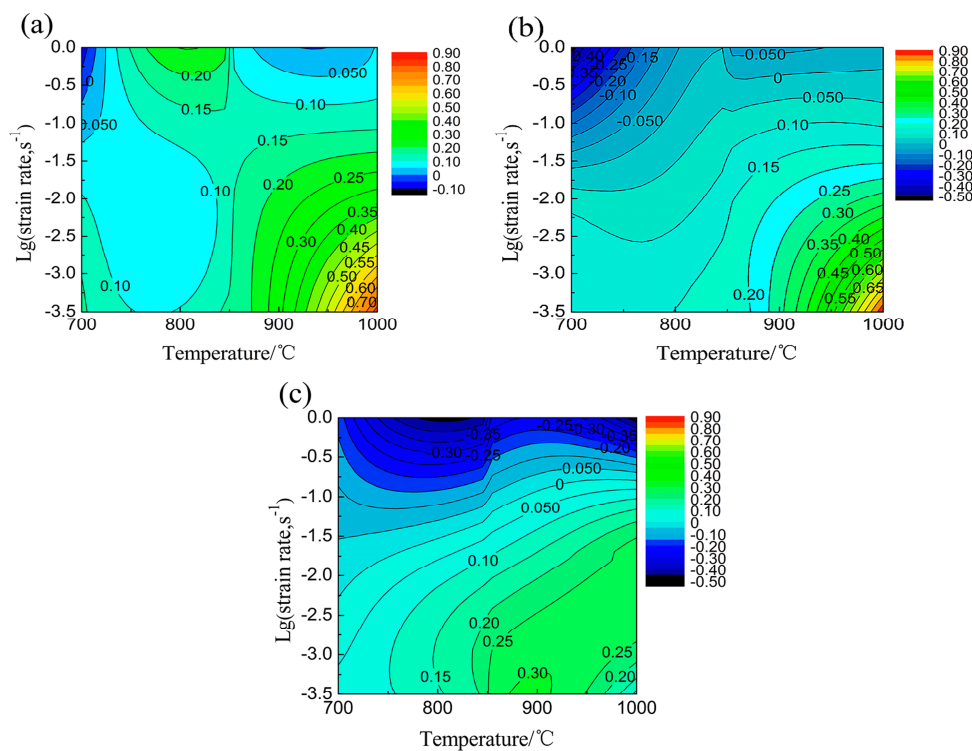
Figure 6. Instability maps of NiTiNb SMA based on various strains: (**a**) $\varepsilon = 0.3$; (**b**) $\varepsilon = 0.6$; and (**c**) $\varepsilon = 0.9$.

The processing map is established on the basis of the power dissipation map and the instability map, as illustrated in Figure 7. In Figure 7, the instability zone is designated in blue, but the stability zone is represented in white. It can be observed that the instability region of NiTiNb SMA increases with increasing true strain. The phenomenon further demonstrates that the workability of NiTiNb SMA becomes worse and worse along with increasing deformation extent. In addition, the instability zone of NiTiNb SMA mainly focuses on the region with high strain rate. In particular, as for the true strain of 0.9, the instability zone of NiTiNb SMA is mainly concentrated on the region with high strain rate. Furthermore, the strain rate range, which represents the stability zone, decreases with decreasing deformation temperature. This indicates that the lower deformation temperature leads to the poorer workability of NiTiNb SMA. However, the stability zone is not completely suitable for hot working of NiTiNb SMA, as well. In general, the high value of η in the stable working zone indicates that the larger fraction of energy is dissipated during microstructural evolution of NiTiNb SMA subjected to plastic deformation at high temperatures, such as dynamic recrystallization, dynamic recovery and phase transformation. Therefore, the higher η value is more suitable for hot working. In addition, it can be found from Figure 7c that the higher η value, which represents the stability zone, is located in two regions. One region means that NiTiNb SMA experiences hot working in the temperature range of 750–840 °C, as well as at the strain rate range of 0.0003–0.001 s^{-1}. The other region indicates that NiTiNb SMA is subjected to hot working in the temperature range of 930–1000 °C, as well as at the strain rate range of 0.016–0.1 s^{-1}. As a consequence, the aforementioned high η value in the stability zone is considered to represent the optimum hot working zone of NiTiNb SMA. In addition, there exist some zones, which possess very low η value in the stability region. The phenomenon indicates that when NiTiNb SMA is subjected to hot working in the regions with very low η values, although the severe working defects should not be formed, the inhomogeneous microstructure defects can be induced. Therefore, it is more appropriate for NiTiNb SMA not to be subjected to hot working in the stability regions with very low η value. In particular, when NiTiNb SMA is subjected to hot working in the instability regions, the severe microstructure defects are induced, as shown in Figure 8. It is

obviously observed from Figure 8 that coarsening grains, band microstructure, and intercrystalline overfiring appear in the microstructures of the deformed NiTiNb SMA. These microstructure defects have an adverse impact on the properties of NiTiNb SMA.
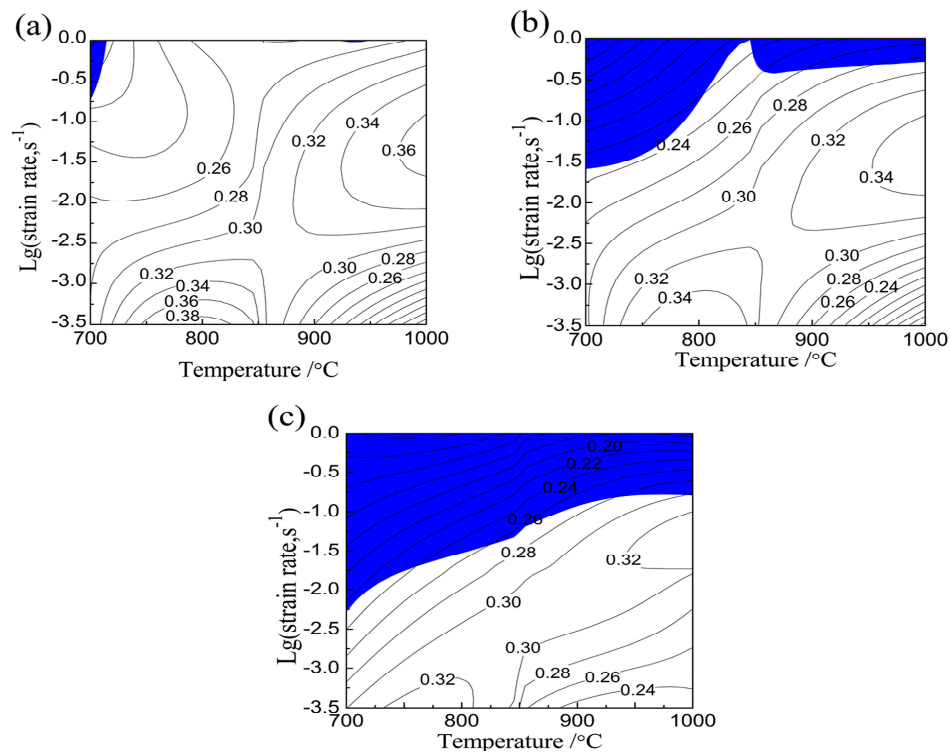

Figure 7. Processing maps of NiTiNb SMA based on various strains: (**a**) $\varepsilon = 0.3$; (**b**) $\varepsilon = 0.6$; and (**c**) $\varepsilon = 0.9$. The blue color in the figure represents the instability region.
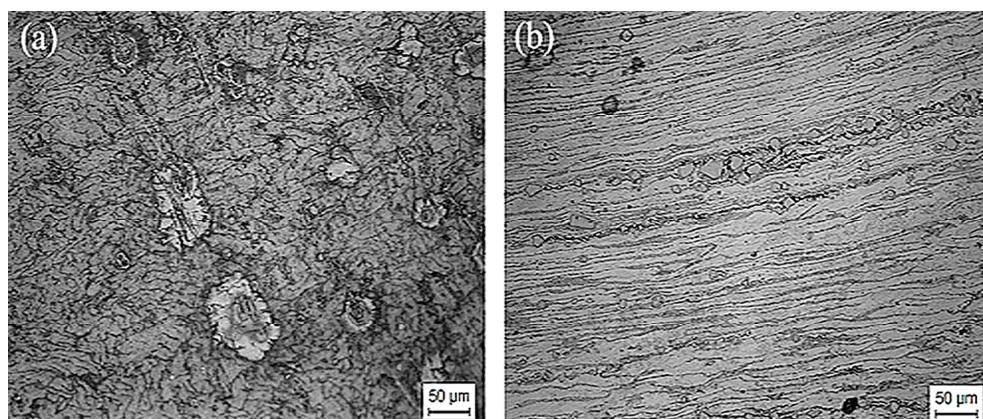

Figure 8. Microstructures of NiTiNb SMA undergoing compression at 1000 °C and at 0.05 s^{-1}: (**a**) coarsening grain; and (**b**) band microstructure and intercrystalline overfiring.

5. Conclusions

Based on true stress-strain curves of NiTiNb SMA during uniaxial compression deformation at temperatures ranging from 700 to 1000 °C, and at strain rates ranging from 0.0005 to 0.5 s^{-1}, according to the values of flow stresses corresponding to true strains of 0.3, 0.6, and 0.9, a processing map of NiTiNb SMA is established based on the dynamic material model (DMM) principle. As a consequence, the following conclusions are drawn:

(1)　Flow stress of NiTiNb SMA is dependent upon the strain rate and temperature. In the case of a constant strain rate, flow stress decreases with increasing temperature. In the case of a constant temperature, flow stress increases with the increasing strain rate. The instability region of NiTiNb SMA increases with the increasing true strain and it mainly focuses on the region with high strain rate. The workability of NiTiNb SMA becomes worse and worse with increasing plastic strain, as well as decreasing the deformation temperature.

(2)　There exist two stability zones which are suitable for hot working of NiTiNb SMA. One is the region where NiTiNb SMA experiences hot working in the temperature range of 750–840 °C, as well as at the strain rate range of 0.0003–0.001 s^{-1}. The other is the region where NiTiNb SMA is subjected to hot working in the temperature range of 930–1000 °C, as well as at the strain rate range of 0.016–0.1 s^{-1}. The processing map lays the foundation for optimizing the hot working parameters of NiTiNb SMA.

Author Contributions: Yu Wang wrote the manuscript and performed the XRD analysis, OM observation, and compression test; Shuyong Jiang supervised the manuscript; and Yanqiu Zhang established the processing map.

References

1.　Jani, J.M.; Leary, M.; Subic, A.; Gibson, M.A. A review of shape memory alloy research, applications and opportunities. *Mater. Des.* **2014**, *56*, 1078–1113. [CrossRef]

2.　Elibol, C.; Wagner, M.F.X. Investigation of the stress-induced martensitic transformation in pseudoelastic NiTi under uniaxial tension, compression and compression-shear. *Mater. Sci. Eng. A* **2015**, *621*, 76–81. [CrossRef]

3.　Kuang, C.H.; Chien, C.; Wu, S.K. Multistage martensitic transformation in high temperature aged Ti$_{48}$Ni$_{52}$ shape memory alloy. *Intermetallics* **2015**, *67*, 12–18. [CrossRef]

4.　Jones, N.G.; Dye, D. Influence of applied stress on the transformation behaviour and martensite evolution of a Ti-Ni-Cu shape memory alloy. *Intermetallics* **2013**, *32*, 239–249. [CrossRef]

5.　Basu, R.; Eskandari, M.; Upadhayay, L.; Mohtadi-Bonab, M.A.; Szpunar, J.A. A systematic investigation on the role of microstructure on phase transformation behavior in Ni-Ti-Fe shape memory alloys. *J. Alloys Compd.* **2015**, *645*, 213–222. [CrossRef]

6.　Mohammad Sharifi, E.; Kermanpur, A.; Karimzadeh, F. The effect of thermomechanical processing on the microstructure and mechanical properties of the nanocrystalline TiNiCo shape memory alloy. *Mater. Sci. Eng. A* **2014**, *598*, 183–189. [CrossRef]

7.　Jiang, P.C.; Zheng, Y.F.; Tong, Y.X.; Chen, F.; Tian, B.; Li, L.; Gunderov, D.V.; Valiev, R.Z. Transformation hysteresis and shape memory effect of an ultrafine-grained TiNiNb shape memory alloy. *Intermetallics* **2014**, *54*, 133–135. [CrossRef]

8.　Choi, E.; Hong, H.K.; Kim, H.S.; Chung, Y.S. Hysteretic behavior of NiTi and NiTiNb SMA wires under recovery or pre-stressing stress. *J. Alloys Compd.* **2013**, *577*, 444–447. [CrossRef]

9.　Zhao, L.C.; Duerig, T.W.; Justi, S. The study of niobium-rich precipitates in a Ni-Ti-Nb shape memory alloy. *Scr. Metall. Mater.* **1990**, *24*, 221–226. [CrossRef]

10.　Dong, Z.Z.; Zhou, S.L.; Liu, W.X. A study of NiTiNb shape-memory alloy pipe-joint with improved properties. *Mater. Sci. Forum* **2002**, *394–395*, 107–110. [CrossRef]

11.　Uchida, K.; Shigenaka, N.; Sakuma, T.; Sutou, Y.; Yamauchi, K. Effect of Nb content on martensitic transformation temperatures and mechanical properties of Ti-Ni-Nb shape memory alloys for pipe joint applications. *Mater. Trans.* **2007**, *48*, 445–450. [CrossRef]

12.　Korostelev, A.B. Properties of a Ti-Ni-Nb Alloy for producing thermomechanical couplings. *Russ. Metall.* **2011**, *2011*, 576–578. [CrossRef]

13.　Etaati, A.; Dehghani, K. A study on hot deformation behavior of Ni-42.5Ti-7.5Cu alloy. *Mater. Chem. Phys.* **2013**, *140*, 208–215. [CrossRef]

14.	Mirzadeh, H.; Parsa, M.H. Hot deformation and dynamic recrystallization of NiTi intermetallic compound. *J. Alloys Compd.* **2014**, *614*, 56–59. [CrossRef]

15.	Yeom, J.T.; Kim, J.H.; Hong, J.K.; Kim, S.W.; Park, C.H.; Nam, T.H.; Lee, K.Y. Hot forging design of as-cast NiTi shape memory alloy. *Mater. Res. Bull.* **2014**, *58*, 234–238. [CrossRef]

16.	Morakabati, M.; Kheirandish, S.; Aboutalebi, M.; Taheri, A.K.; Abbasi, S.M. The effect of Cu addition on the hot deformation behavior of NiTi shape memory alloys. *J. Alloys Compd.* **2010**, *499*, 57–62. [CrossRef]

17.	Morakabati, M.; Aboutalebi, M.; Kheirandish, S.; Taheri, A.K.; Abbasi, S.M. Hot tensile properties and microstructural evolution of as cast NiTi and NiTiCu shape memory alloys. *Mater. Des.* **2011**, *32*, 406–413. [CrossRef]

18.	Shamsolhodaei, A.; Zarei-hanzaki, A.; Ghambari, M.; Moemeni, S. The high temperature flow behavior modeling of NiTi shape memory alloy employing phenomenological and physical based constitutive models: A comparative study. *Intermetallics* **2014**, *53*, 140–149. [CrossRef]

19.	Zhang, Y.Q.; Jiang, S.Y.; Zhao, Y.N.; Liu, S.W. Constitutive equation and processing map of equiatomic NiTi shape memory alloy under hot plastic deformation. *Trans. Nonferr. Met. Soc.* **2016**, *26*, 2152–2161. [CrossRef]

20.	Zhang, Y.; Jiang, S.; Chen, C.; Hu, L.; Zhu, X. Hot workability of a NiTiCu shape memory alloy with acicular martensite phase based on processing maps. *Intermetallics* **2017**, *86*, 94–103. [CrossRef]

21.	Gangolu, S.; Gourav Rao, A.; Sabirov, I.; Kashyap, B.P.; Prabhu, N.; Deshmukh, V.P. Development of constitutive relationship and processing map for Al-6.65Si-0.44Mg alloy and its composite with B_4C particulates. *Mater. Sci. Eng. A* **2016**, *655*, 256–264. [CrossRef]

22.	Rastegari, H.; Kermanpur, A.; Najafizadeh, A.; Somani, M.C.; Porter, D.A.; Ghassemali, E.; Jarfors, A.E.W. Determination of processing maps for the warm working of vanadium microalloyed eutectoid steels. *Mater. Sci. Eng. A* **2016**, *658*, 167–175. [CrossRef]

23.	Rajput, S.K.; Chaudhari, G.P.; Nath, S.K. Characterization of hot deformation behavior of a low carbon steel using processing maps, constitutive equations and Zener-Hollomon parameter. *J. Mater. Process. Technol.* **2016**, *237*, 113–125. [CrossRef]

24.	Momeni, A.; Dehghani, K. Hot working behavior of 2205 austenite-ferrite duplex stainless steel characterized by constitutive equations and processing maps. *Mater. Sci. Eng. A* **2011**, *528*, 1448–1454. [CrossRef]

25.	Prasad, Y.V.R.K.; Sasidhara, S. *Hot Working Guide: A Compendium of Processing Maps*; ASM International: Materials Park, OH, USA, 1997.

26.	Wu, H.; Wu, C.; Yang, J.; Lin, M. Hot workability analysis of AZ61 Mg alloys with processing maps. *Mater. Sci. Eng. A* **2014**, *607*, 261–268. [CrossRef]

27.	Shang, X.; Zhou, J.; Wang, X.; Luo, Y. Optimizing and identifying the process parameters of AZ31 magnesium alloy in hot compression on the base of processing maps. *J. Alloys Compd.* **2015**, *629*, 155–161. [CrossRef]

28.	Wu, H.; Wen, S.P.; Huang, H.; Gao, K.Y.; Wu, X.L.; Wang, W.; Nie, Z.R. Hot deformation behavior and processing map of a new type Al-Zn-Mg-Er-Zr alloy. *J. Alloys Compd.* **2016**, *685*, 869–880. [CrossRef]

29.	Zeng, W.D.; Zhou, Y.G.; Zhou, J.; Yu, H.Q.; Zhang, X.M.; Xu, B. Recent development of processing map theory. *Rare Met. Mater. Eng.* **2006**, *35*, 673–677.

30.	Ziegler, H.; Sneedon, I.N.; Hill, R. *Progress in Solid Mechanics*; Wiley: New York, NY, USA, 1963.

31.	Łukaszek-Solek, A.; Krawczyk, J. The analysis of the hot deformation behaviour of the Ti-3Al-8V-6Cr-4Zr-4Mo alloy, using processing maps, a map of microstructure and of hardness. *Mater. Des.* **2015**, *65*, 165–173. [CrossRef]